S1 ADCIRC v55 Formulation and Solution Scheme

S1.1 Reformulation of Governing Equations

To facilitate a Continuous Galerkin Finite Element Method (CG-FEM) solution to the governing equations in spherical coordinates (Eqs. (1)-(3) from the main manuscript) with minimal modification to FEM methods that exist for Cartesian coordinates we use a rectilinear mapping projection. Previously in ADCIRC, the Carte Parallelogrammatique projection (CPP) has been used (Kolar et al., 1994a), which is an equidistant cylindrical projection that is neither area preserving (equal-area) nor angle preserving (conformal). In the TELEMAC model a conformal cylindrical Mercator projection is used (Hervouet, 2007). Here, the formulation is generalized to a choice of equal-area, equidistant, and conformal cylindrical projections. The projections $P : (\lambda, \phi) \rightarrow (x, y)$ considered are characterized by that $x = a\lambda + b$ (a and b are a constant) and $y = y(\phi)$, i.e. the horizontal coordinate x depends linearly only on the longitude λ and the vertical coordinate y only on the latitude ϕ. The various specific cylindrical projections may be written as,

$$x = R(\lambda - \lambda_0)\cos\phi_0, \quad y = \begin{cases} R\sin\phi\sec\phi_0 & : \text{equal-area} \\ R\phi & : \text{equidistant (CPP)} \\ R\ln(\tan\phi + \sec\phi)\cos\phi_0 & : \text{Mercator (conformal)} \end{cases} \tag{S1}$$

where (λ_0, ϕ_0) is the arbitrary projection origin. Using the cylindrical projections of the form considered, it can be shown that the governing equations (Eqs. (1)-(3) from the main manuscript) can be cast into an equivalent set of equations, a form reminiscent of the standard SWE in the Cartesian coordinate system, as follows,

$$\frac{\partial(S_o\zeta)}{\partial t} = -\frac{\partial(S_1 U H)}{\partial x} - \frac{\partial(V H \cos\phi)}{\partial y} \tag{S2}$$

$$\frac{\partial U}{\partial t} + S_x g \frac{\partial\zeta}{\partial x} = -S_x U \frac{\partial U}{\partial x} - S_y V \frac{\partial U}{\partial y} - S_x \frac{\partial\Psi}{\partial x} - (\mathcal{C}_{xy} - f')V + \frac{\tau_w U_w}{\rho_0 H} - \left(\frac{\tau_b}{\rho_0 H} + \mathcal{C}_{xx}\right)U$$

$$+ \frac{1}{H}\left[S_x \frac{\partial\tau_{xx}}{\partial x} + S_y \frac{\partial\tau_{xy}}{\partial y} - \frac{1}{R}\tan\phi(\tau_{xy} + \tau_{yx})\right] \tag{S3}$$

$$\frac{\partial V}{\partial t} + S_y g \frac{\partial\zeta}{\partial y} = -S_x U \frac{\partial V}{\partial x} - S_y V \frac{\partial V}{\partial y} - S_y \frac{\partial\Psi}{\partial y} - (\mathcal{C}_{yx} + f')U + \frac{\tau_w V_w}{\rho_0 H} - \left(\frac{\tau_b}{\rho_0 H} + \mathcal{C}_{yy}\right)V$$

$$+ \frac{1}{H}\left[S_x \frac{\partial\tau_{yx}}{\partial x} + S_y \frac{\partial\tau_{yy}}{\partial y} + \frac{1}{R}\tan\phi(\tau_{xx} - \tau_{yy})\right] \tag{S4}$$

where

$$\tau_{xx} = 2\nu_t S_x H \frac{\partial U}{\partial x}, \quad \tau_{xy} = \nu_t H\left(S_y \frac{\partial U}{\partial y} + S_x \frac{\partial V}{\partial x}\right) \quad \text{or} \quad \nu_t S_x H \frac{\partial V}{\partial x}$$

$$\tau_{yy} = 2\nu_t S_y H \frac{\partial V}{\partial y}, \quad \tau_{yx} = \nu_t H\left(S_y \frac{\partial U}{\partial y} + S_x \frac{\partial V}{\partial x}\right) \quad \text{or} \quad \nu_t S_y H \frac{\partial U}{\partial y}$$

$$\mathcal{C} = \begin{pmatrix} \mathcal{C}_{xx} & \mathcal{C}_{xy} \\ \mathcal{C}_{yx} & \mathcal{C}_{yy} \end{pmatrix} \approx \begin{pmatrix} \mathcal{C}_{\lambda\lambda} & \mathcal{C}_{\lambda\phi} \\ \mathcal{C}_{\phi\lambda} & \mathcal{C}_{\phi\phi} \end{pmatrix}.$$

and the spherical correction factors

$$S_x = \frac{1}{R\cos\phi}\frac{\partial x}{\partial\lambda}, \quad S_y = \frac{1}{R}\frac{\partial y}{\partial\phi}, \quad S_0 = \frac{\cos\phi}{S_y}, \quad \text{and} \quad S_1 = S_x S_0. \tag{S5}$$

It can be verified that these correction factors are a function of ϕ (and hence of y) only; their values depend on the formula of the projection considered. For the projections given in (S1), these factors correspond to

$$S_0 = (\sec\phi_0)^{p-1}(\cos\phi)^p, \quad S_1 = (\sec\phi_0)^{p-2}(\cos\phi)^{p-1}, \quad S_x = \cos\phi_0\sec\phi, \quad \text{and} \quad S_y = (S_x)^{p-1}$$

1

30 with the integer exponent p equal to 0, 1, and 2 for the equal area, equidistant, and Mercator projections, respectively.

In order to avoid the node-to-node oscillations arising from directly applying the CG-FEM to the primitive continuity equation (Gray and Lynch, 1979), the continuity equation is reformulated into the so-called Generalized Wave Continuity Equation (GWCE) (Kinnmark, 1986; Westerink et al., 1992; Le Bars et al., 2010). The GWCE is obtained by differentiating the primitive continuity Eq. (S2) with respect to time, adding on Eq. (S2) multiplied by a constant and positive weight, τ_0, and using (S3)

35 and (S4) to eliminate $\frac{\partial U}{\partial t}$ and $\frac{\partial V}{\partial t}$. This leads to

$$\frac{\partial^2(S_0\zeta)}{\partial t^2} + \tau_0\frac{\partial(S_0\zeta)}{\partial t} - \frac{\partial}{\partial x}\left(S_1 S_x gH\frac{\partial\zeta}{\partial x}\right) - \frac{\partial}{\partial y}\left(S_y\cos\phi gH\frac{\partial\zeta}{\partial y}\right) + \frac{\partial}{\partial x}(S_1\widetilde{J}_x) + \frac{\partial}{\partial y}(\cos\phi\widetilde{J}_y) = 0 \tag{S6}$$

$$\widetilde{J}_x = \tau_0 UH + U\frac{\partial\zeta}{\partial t} + H\times(\text{RHS of (S3)}) \tag{S7}$$

$$\widetilde{J}_y = \tau_0 VH + V\frac{\partial\zeta}{\partial t} + H\times(\text{RHS of (S4)}) \tag{S8}$$

The final set of equations that are actually solved by ADCIRC v55 are Eqs. (S3), (S4), and (S6).

40 ## S1.2 Comparison to Previous Formulation

The form of the primitive continuity equation in Eq. (S2), and hence the GWCE in Eq. (S6), differs from the previously employed formulation in ADCIRC by multiplying both sides of the continuity equation (Eq. (1) of the main manuscript) in the cylindrical-projection coordinates,

$$\frac{\partial\zeta}{\partial t} = -S_x\frac{\partial UH}{\partial x} - \frac{S_y}{\cos\phi}\frac{\partial VH\cos\phi}{\partial y}, \tag{S9}$$

45 by $\cos\phi/S_y$, thus the cancellation of the factor in the second term in the RHS of the equation. On the other hand, the previous versions of ADCIRC considers (the GWCE derived from) (S9) with the manipulation to be described shortly below. It is worth nothing that the factor $\frac{S_y}{\cos\phi}$ depends on ϕ and therefore the second term in the RHS of (S9) poses some issues: (i) it does not permit an immediate application of SWE for the Cartesian coordinates (not without relatively large efforts in code modifications), (ii) the second-derivative operator in the GWCE derived straightforwardly from (S9) is no longer a self-adjoint operator,

50 thus contributing additional difficulty in solving a system of algebraic equations arising from the FEM discretization (with the semi-implicit time stepping), and (iii) discrete mass conservation cannot be attained from (S9), and hence its associated GWCE. Note that the issue (iii) is arguably a more concerning issue than (i) and (ii) which are merely nuisances. ADCIRC uses the equivalent form of (S9) that is free of the above mentioned issue (i) and (ii) (and (iii) by omitting a specific term to be mentioned below) through the use of the product rule to further expand the second term in the RHS (Kolar et al., 1994a),

55 $$\frac{\partial\zeta}{\partial t} = -\frac{\cos\phi_0}{\cos\phi}\frac{\partial UH}{\partial x} - \frac{\partial VH}{\partial y} - \frac{\tan\phi}{R}VH. \tag{S10}$$

Note that the CPP projection, adopted by previous ADCIRC versions, are used in the above equation. Except for the additional source term, this form (S10) resembles even more closely to the SWE in the Cartesian coordinates than Eq. (S2) does. However, the appearance of the $(\tan\phi/R)VH$ source term on the RHS is problematic as it approaches infinity near the poles resulting in the stiff source term. Furthermore, since (S10) has the form a balance equation with this source term, its solution in the

60 FEM using the GWCE does not lead to mass conservation (in terms of total water volume). In fact, we attempt to solve this form of the equations and found it to be inherently unstable for simulation. Indeed, current and previous official versions of ADCIRC omit this term (and the terms with the factor $\tan\phi$ in the momentum equations (S3) and (S4)). With this omission the equations solved takes into account the Earth's curvature only partially. This is acceptable and can be justified for local or regional domains in equatorial and mid-latitude areas (ADCIRC has traditionally been used to simulate the Western North

65 Atlantic regional domain), but certainly not global domains.

In contrast, the form of Eq. (S2) presented here avoids the need to expand out the second RHS term of Eq. (S2) because the factor $\frac{S_y}{\cos\phi}$ cancel out by means of multiplying through by its inverse. It can also be observed the second derivative terms in

(S6) (specifically, the third and forth terms) form a self-adjoint operator; therefore, their FEM discrete equations are symmetric. Furthermore, Eq. (S2) has the form of a conservation law equation, an important aspect to realize discrete mass conservation (cf. Hervouet, 2007; Castro et al., 2018) (in the global sense for the CG-FEM). The only minor inconvenience arises from the requirement to deal with $S_0\zeta$ in the time derivative term of Eq. (S2) instead of ζ. However, in practice S_0 may be lumped in with other coefficients on the left-hand side to recover ζ directly if we set S_0 to be constant across an element.

S1.3 Coordinate Rotation to Remove Pole Singularity

Even though a mesh can be generated on the sphere to cover the entire Earth, the spherical coordinate system prohibits the placement of a vertex on a pole due to the appearance of a singularity, and the cylindrical mapping system adopted by the numerical model precludes any element from covering over a pole (Fig. S1). To avoid this problem, FVCOM locally switches to the stereographic projection in the vicinity of the North Pole (Chen et al., 2016). Alternatively, the governing equations can be formulated in terms of local coordinates avoiding the spherical coordinate form altogether (Comblen et al., 2009). Here, by taking advantage of the current positioning of Earth's landmasses (antipodes), we consider a coordinate system resulting from the rigid rotation of axes so that the North and South pole of the rotated coordinate system both pass through land. As a result, the singularity in the governing equations at the new poles is no longer part of the ocean domain, hence sidestepping the pole problem. Fig. S1(c) depicts a computational mesh in the Mercator projection associated with a rotated coordinate system with its computational North and South pole passing through Greenland and Antarctica, respectively. The governing equations in the rotated coordinate system are identical to (1)-(3) of the main manuscript where the vector components (velocity and 10-m wind velocity) are now understood as the components associated with the rotated coordinate system and the Coriolis components in the λ'- and ϕ'- momentum equations are determined by,

$$-2\Omega'_r V', \quad \text{and} \quad 2\Omega'_r U', \tag{S11}$$

respectively (here, the prime superscript is used to distinguish the rotated coordinate system from the original coordinate system). In the above equation, $\Omega'_r = \Omega(\mathcal{R}_{13}\cos\phi'\cos\lambda' + \mathcal{R}_{23}\cos\phi'\sin\lambda' + \mathcal{R}_{33}\sin\phi')$ where $\mathcal{R}_{ij}$ denotes the $(i,j)^{\text{th}}$-entry of the 3×3 rotation matrix $\mathbf{R}$ that maps the Cartesian coordinates (x,y,z) of the original coordinate system to (x',y',z') of the rotated coordinate system through,

$$[x'\,y'\,z']^T = \mathbf{R}[x\,y\,z]^T, \quad \mathbf{R} = \begin{bmatrix} \mathcal{R}_{11} & \mathcal{R}_{12} & \mathcal{R}_{13} \\ \mathcal{R}_{21} & \mathcal{R}_{22} & \mathcal{R}_{23} \\ \mathcal{R}_{31} & \mathcal{R}_{32} & \mathcal{R}_{33} \end{bmatrix}. \tag{S12}$$

It can be verified that, at a given point, the value of the Coriolis parameter $2\Omega'_r$ in the rotated coordinate frame is identical to that of the original coordinate frame, more precisely, $2\Omega'_r = 2\Omega\sin(\phi(\lambda',\phi'))$ where $\phi(\lambda',\phi)$ denotes a coordinate transformation mapping (λ',ϕ') to ϕ.

An implementation of the coordinate rotation involves relatively minor modifications in the code and amounts simply to: (i) (pre-)computing, with a user-provided rotation matrix $\mathbf{R}$, the new (λ',ϕ') and its cylindrical projection coordinates from the longitude-latitude coordinate (λ,ϕ) and the Coriolis parameter Ω'_r; and (ii) during the time-stepping, rotating the 10-m wind vector components and the internal tide wave drag tensor in Eqs. (S3), (S4) and, when output velocity is required, rotating the (λ',ϕ')-velocity components back to the original longitude-latitude coordinate system. Note that, for a given vector, its radial and angular components $[W'\,U'\,V']^T$ in the rotated coordinate system (r',λ',ϕ') can be obtained by multiplying its components $[W\,U\,V]^T$ in the non-rotated coordinate system (r,λ,ϕ) by a following matrix $\mathbf{T}$ (and *vice versa* through $\mathbf{T}^{-1}$),

$$\mathbf{T} = \mathbf{R}_s(\lambda',\phi')\mathbf{R}\mathbf{R}_s(\lambda,\phi)^T, \quad \mathbf{R}_s = \begin{bmatrix} \cos\phi\cos\lambda & \cos\phi\sin\lambda & \sin\phi \\ -\sin\lambda & \cos\lambda & 0 \\ -\sin\phi\cos\lambda & -\sin\phi\sin\lambda & \cos\phi \end{bmatrix} \tag{S13}$$

where $\mathbf{R}$ denotes the rotation matrix and $\mathbf{R}_s(\lambda,\phi)$ denotes a matrix arising from expressing the unit vectors $\widehat{\mathbf{e}}_r$, $\widehat{\mathbf{e}}_\lambda$, and $\widehat{\mathbf{e}}_\phi$ in the spherical coordinate system in terms of the unit vectors $\widehat{\mathbf{i}}$, $\widehat{\mathbf{j}}$, and $\widehat{\mathbf{k}}$ of the Cartesian coordinate system. Note that $\mathbf{R}_s$ and (by definition) $\mathbf{R}$ are an orthogonal matrix; as a result, $\mathbf{T}$ is an orthogonal matrix and thus can be trivially inverted. Furthermore,

it can be shown, as expected, that all entries of the first row and column of $\mathbf{T}$ are vanishing except for the $(1,1)^{\text{th}}$ entry $[\mathbf{T}]_{(1,1)}$ which is equal to unity. Thus, the lower 2×2 submatrix of $\mathbf{T}$ is sufficient for going back and forth between the horizontal components of a vector in the rotated and original coordinate system.

S1.4 Numerical Solution Scheme

In numerical solution of Eqs. (S6), (S3), and (S4), the linear CG-FEM is used in a spatial discretization while finite-difference schemes are used in temporal discretization. Readers are referred to Luettich and Westerink (2004) for details on the CG-FEM spatial discretization. Here, we present the temporal integration solution scheme of Eqs. (S3)-(S6). For computational efficiency, the scheme allows for the momentum equations to be decoupled from the GWCE and solved separately in succession. First, the GWCE equations are solved for $\zeta^{*s+1} \equiv \zeta^{s+1} - \zeta^s$ (s indicates the time level) using a three time level approximation of ζ in the gravity wave term ($gH\frac{\partial \zeta}{\partial x}$). The solution of the GWCE equations are of the form:

$$\frac{S_0 \zeta^{*s+1}}{\Delta t}\left[\frac{1}{\Delta t} + \frac{\tau_0}{2}\right] + \alpha_1 \text{GW}(\zeta^{*s+1}) = \frac{S_0 \zeta^{*s}}{\Delta t}\left[\frac{1}{\Delta t} - \frac{\tau_0}{2}\right]$$
$$- (\alpha_1 + \alpha_2)\text{GW}(\zeta^s) - \alpha_3 \text{GW}(\zeta^{s-1}) + \frac{\partial(S_1 \tilde{J}_x{}^s)}{\partial x} + \frac{\partial(\tilde{J}_y{}^s \cos\phi)}{\partial y} \tag{S14}$$

$$\text{GW}(z) = -\frac{\partial}{\partial x}\left(S_1 S_x gH \frac{\partial z}{\partial x}\right) - \frac{\partial}{\partial y}\left(S_y gH \cos\phi \frac{\partial z}{\partial y}\right). \tag{S15}$$

In the previous versions of ADCIRC, the GW terms include only the linear components of the pressure gradients (i.e., $gh\frac{\partial \zeta}{\partial x}$ and $gh\frac{\partial \zeta}{\partial y}$) while the nonlinear components of the pressure gradients (i.e., $g\zeta\frac{\partial \zeta}{\partial x}$ and $g\zeta\frac{\partial \zeta}{\partial y}$) are treated explicitly at time level s. As a consequence of h being time independent, this strategy can reduce computational cost since it is not necessary to reassemble the LHS matrix when there is no change in the wetting-drying status. However, the matrix must be updated when wetting-drying is invoked, and we find that solving the full GW term (i.e., $gH\frac{\partial \zeta}{\partial x}$) implicitly aids stability allowing for a larger time step to be employed. Equation (S14) is solved using a conjugate gradient iterative solver when $\alpha_1 > 0$ and/or when using consistent mass-matrix exact integration (Tanaka et al., 2011). Alternatively, when a fully explicit scheme is considered (by setting $\alpha_1 = 0$, $\alpha_2 = 1$, $\alpha_3 = 0$) for an efficiency reason, lumped mass nodal integration may be used to avoid solving the system of linear equations (Tanaka et al., 2011).

Second, the momentum equations are solved for U^{s+1} and V^{s+1} using a symmetrical two time level - Crank-Nicholson type - scheme which has been found to be free from numerical artifacts (Kinnmark, 1986),

$$U^{s+1}\left[\frac{1}{\Delta t} + \frac{1}{2}\left(\frac{\tau_b}{\rho_0 H} + \mathcal{C}_{xx}\right)^s\right] + V^{s+1}\frac{(\mathcal{C}_{xy} - f')^s}{2} = U^s\left[\frac{1}{\Delta t} - \frac{1}{2}\left(\frac{\tau_b}{\rho_0 H} + \mathcal{C}_{xx}\right)^s\right] - V^s\frac{(\mathcal{C}_{xy} - f')^s}{2}$$
$$+ \frac{1}{2}\left[\left(\frac{\tau_w U_w}{\rho_0 H}\right)^{s+1} + \left(\frac{\tau_w U_w}{\rho_0 H}\right)^s\right] - \frac{S_x}{2}\left[\frac{\partial(g\zeta^{s+1} + \Psi^{s+1})}{\partial x} + \frac{\partial(g\zeta^s + \Psi^s)}{\partial x}\right]$$
$$- U^s S_x \frac{\partial U^s}{\partial x} - V^s S_y \frac{\partial U^s}{\partial y} + \frac{1}{H^s}\left[S_x \frac{\partial \tau_{xx}^s}{\partial x} + S_y \frac{\partial \tau_{xy}^s}{\partial y} - \frac{1}{R}\tan\phi(\tau_{xy}^s + \tau_{yx}^s)\right] \tag{S16}$$

$$V^{s+1}\left[\frac{1}{\Delta t} + \frac{1}{2}\left(\frac{\tau_b}{\rho_0 H} + \mathcal{C}_{yy}\right)^s\right] + U^{s+1}\frac{(\mathcal{C}_{yx} + f')^s}{2} = V^s\left[\frac{1}{\Delta t} - \frac{1}{2}\left(\frac{\tau_b}{\rho_0 H} + \mathcal{C}_{yy}\right)^s\right] - U^s\frac{(\mathcal{C}_{yx} + f')^s}{2}$$
$$+ \frac{1}{2}\left[\left(\frac{\tau_w V_w}{\rho_0 H}\right)^{s+1} + \left(\frac{\tau_w V_w}{\rho_0 H}\right)^s\right] - \frac{S_y}{2}\left[\frac{\partial(g\zeta^{s+1} + \Psi^{s+1})}{\partial y} + \frac{\partial(g\zeta^s + \Psi^s)}{\partial y}\right]$$
$$- U^s S_x \frac{\partial V^s}{\partial x} - V^s S_y \frac{\partial V^s}{\partial y} + \frac{1}{H^s}\left[S_y \frac{\partial \tau_{yy}^s}{\partial y} + S_x \frac{\partial \tau_{yx}^s}{\partial x} + \frac{1}{R}\tan\phi(\tau_{xx}^s - \tau_{yy}^s)\right] \tag{S17}$$

with, the now known, ζ^{s+1} obtained from the GWCE solution step (S14). In ADCIRC, a mass lumping is employed in evaluating the FEM spatial discretization of the LHS terms of the above equations (Luettich and Westerink, 2004). As a consequence,
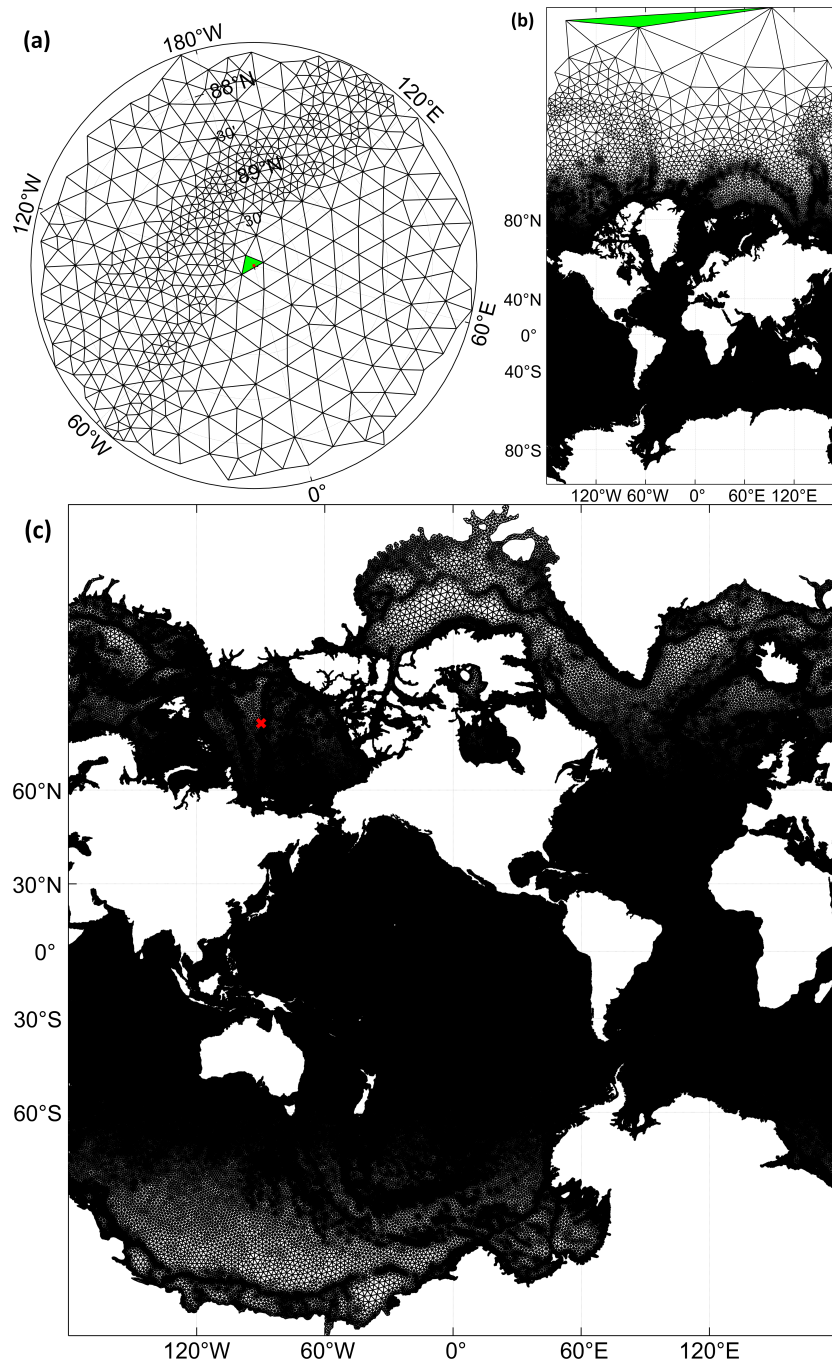
Figure S1. Triangulations of the MinEle-C mesh design (refer to the main manuscript for design details). (a) Stereographic projection zoom-in to the North Pole (red dot) with the element covering the North Pole colored green; (b) Mercator projection showing that the green colored element from (a) becomes flat on the cylindrical mapping system; (c) Mercator projection of the rotated mesh that places the new North Pole in the center of Greenland; the red cross indicates the new position of the centroid of the green color element in (a).

5

the FEM equations of (S16) and (S17) can be solved in a node-by-node fashion, thus reducing the computational time as solving the full mass matrix is avoided.

Owing to the above mentioned solution strategies, ADCIRC is able to significantly reduce the computational time associated with FEM models because it requires, in each time step, only one block diagonal matrix-inversion in the GWCE solution step when using the semi-implicit scheme/consistent mass matrix.

S1.5 Numerical Stability of the Scheme

In previous research, stability analysis of the numerical scheme has been conducted primarily on the Wave Continuity Equation (WCE) (Lynch and Gray, 1979), which is a special case of the GWCE when $\tau_0 = \tau_b/(\rho_0 H)$. It has been shown that the WCE is third-order accurate and unconditionally stable with the following choice of weighting factors (Lynch and Gray, 1979; Foreman, 1983),

$$\alpha_1 = \alpha_3 = \kappa \geq 1/4, \quad \alpha_2 = 1 - 2\kappa \tag{S18}$$

However, the stability of the solution to the GWCE Eq. (S14) depends strongly on the selection of τ_0 in addition to the weighting factors, $\alpha_{1,2,3}$ (Kinnmark, 1986). In fact, empirical evidence by multiple ADCIRC studies suggests that the choice of weighting factors in Eq. (S18) does not lead to an unconditionally stable scheme. Instead, the time step is bounded by the CFL restriction on the gravity wave speed ($Cr = \sqrt{gH}\Delta t/\Delta x < 1$, in which a practical upper bound of Cr is 0.5 or smaller (Dresback and Kolar, 2002)). It has been suggested this restriction on the stability of the GWCE is dominated by the nonlinear terms (Dresback and Kolar, 2002). Although it is true that nonlinear terms will prohibit unconditional stability, the implicit form of the GW term in Eq. (S14) and of the barotropic pressure gradient term ($g\frac{\partial \zeta}{\partial x}$) in Eqs. (S16), (S17) should remove the CFL restriction. To demonstrate this fact we conduct a von Neumann stability analysis on the one-dimensional (1-D) linear GWCE equations, detailed in Sect. S1.5.1.

Kinnmark (1986) used a von Neumann analysis to show that for the choice of weighting factors in Eq. (S18), the set of equations Eqs. (S21), (S22) are only unconditionally stable when $\tau_0 \leq \tau_b/(\rho_0 h)$. Keep in mind that this means that τ_0 has to be smaller than the *minimum* value of $\tau_b/(\rho_0 h)$ in the computational domain, which is a very strict requirement on τ_0 in deep water (e.g., $\tau_b/(\rho_0 h) \approx 10^{-6}$ s^{-1} if $h = 1000$ m, $C_f = 0.01$, $U = 0.1$ ms^{-1}). Moreover, this requirement is at odds with the suggestion that $\tau_b/(\rho_0 h) < \tau_0 < 10\tau_b/(\rho_0 h)$ for good mass balance and solution properties (Kolar et al., 1994b), where $\tau_b/(\rho_0 h)$ here is the *maximum* value in the computational domain.

Further inspection of Kinnmark's stability equations (Sect. S1.5.1) also reveals that the scheme using the weights in Eq. (S18) is stable for any τ_0 if $Cr \leq 4/3$ when using exact integration (consistent mass matrix). Thus, based on empirical evidence we can assume that in practice models do not satisfy $\tau_0 \leq \tau_b/(\rho_0 h)$ everywhere, and are thus bounded by the aforementioned CFL constraint ($Cr \leq 4/3$ in 1-D, which is typically reduced by a $\sqrt{2}/2$ multiple in 2-D (Kinnmark and Gray, 1984)) when using the choice of weighting factors in Eq. (S18).

To try and circumvent the $\tau_0 \leq \tau_b/(\rho_0 h)$ stability requirement, we propose an alternative (non-centered) weighting scheme,

$$\alpha_1 = \alpha_2 = \kappa, \quad \alpha_3 = 1 - 2\kappa \tag{S19}$$

The aim of this weighting scheme is to place greater weight on the future and current time levels than the previous time level, i.e., improve the implicit nature of the scheme compared to Eq. (S18). In turns out that this scheme is unconditionally stable when using exact integration if:

$$1/3 \leq \kappa \leq 1/2, \qquad \tau_0\Delta t \leq \frac{16}{3}(3\kappa - 1) \tag{S20}$$

hence the strict requirement on τ_0 [$\leq \tau_b/(\rho_0 h)$] for unconditional stability in the centered scheme has been eliminated, with $\kappa = 1/2$ providing the most relaxed constraints for $\tau_0\Delta t$.

S1.5.1 Stability Analysis of the 1-D Linearized GWCE

The linearized 1-D form of Eqs. (S14)-(S17), sans atmospheric and astronomical forcing terms (hence the internal wave drag tensor is also omitted) is as follows,

$$\frac{\zeta^{*s+1}}{\Delta t}\left(\frac{1}{\Delta t}+\frac{\tau_0}{2}\right) - \alpha_1 gh\frac{\partial^2\zeta^{*s+1}}{\partial x^2} = \frac{\zeta^{*s}}{\Delta t}\left(\frac{1}{\Delta t}-\frac{\tau_0}{2}\right)$$

$$+ (\alpha_1+\alpha_2)gh\frac{\partial^2\zeta^s}{\partial x^2} + \alpha_3 gh\frac{\partial^2\zeta^{s-1}}{\partial x^2} + \left(\tau_0 - \frac{\tau_b^s}{\rho_0 h}\right)\frac{\partial U^s}{\partial x} \tag{S21}$$

$$U^{s+1}\left(\frac{1}{\Delta t}+\frac{\tau_b^s}{2\rho_0 h}\right) = U^s\left(\frac{1}{\Delta t}-\frac{\tau_b^s}{2\rho_0 h}\right) - \frac{g}{2}\left(\frac{\partial\zeta^s}{\partial x}+\frac{\partial\zeta^{s+1}}{\partial x}\right) \tag{S22}$$

The last term on the right hand side of Eq. (S21) is responsible for the difference between the WCE and GWCE.

Herein the von Neumann/Fourier stability analysis of the linearized 1-D GWCE Eq. (S21) and non-conservative momentum Eq. (S22) solved using linear finite-elements in space is conducted following Kinnmark (1986). In this analysis, the water depth, h, is assumed to be constant, mesh vertices are assumed to be equally spaced, and the boundary conditions are assumed periodic. The FE spatial-discretization equations of (S21) and (S22) of the weak formula associated with the ith-node test function are as follows

$$(1+T_0)\left(\frac{1}{6}\zeta_{i-1}^{*s+1}+\frac{2}{3}\zeta_i^{*s+1}+\frac{1}{6}\zeta_{i+1}^{*s+1}\right) - \alpha_1 Cr^2\triangle\zeta_i^{*s+1} =$$

$$(1-T_0)\left(\frac{1}{6}\zeta_{i-1}^{*s}+\frac{2}{3}\zeta_i^{*s}+\frac{1}{2}\zeta_{i+1}^{*s}\right) + (\alpha_1+\alpha_2)Cr^2\triangle\zeta_i^{s*} + \alpha_3 Cr^2\triangle\zeta_i^{s-1} + \left(\tau_0 - \frac{\tau_b^s}{\rho_0 h}\right)\frac{\Delta t^2}{2\Delta x}\left(U_{i+1}^s - U_{i-1}^s\right) \tag{S23}$$

$$(1+T_b)U_i^{s+1} + g\frac{\Delta t}{4\Delta x}\left(\zeta_{i+1}^{s+1}+\zeta_{i-1}^{s+1}\right) = (1-T_b)U_i^s - g\frac{\Delta t}{4\Delta x}\left(\zeta_{i+1}^s+\zeta_{i-1}^s\right) \tag{S24}$$

where $Cr = \sqrt{gh}\Delta t/\Delta x$, $T_0 = \tau_0\Delta t/2$, $T_b = \tau_b\Delta t/(2\rho_0 h)$ and $\triangle q_i \equiv q_{i-1}-2q_i+q_{i+1}$ (as outlined in Sect. S1.4, the lumped mass matrix with the trapezoid quadrature rule is used in obtaining the discrete equation of the momentum equation (S24) while the consistent mass matrix is considered in the discretization of the GWCE (S23); the discrete GWCE equation with the mass lumping corresponds simply to replacing the terms in the first parenthesis on the LHS and RHS of (S23) with ζ_i^{*s+1} and ζ_i^{*s}, respectively). Selecting a discrete solution of node j at time level s of the form $(\widehat{\zeta}_\sigma^{*s}, \widehat{\zeta}_\sigma^s, \widehat{u}_\sigma^s)e^{I(j\sigma\Delta x)}$, $I = \sqrt{-1}$ (i.e. the σth harmonic of $(\zeta_j^s, \zeta_j^s, u_j^s)$) yields the following third-order characteristic polynomial equation of the amplification matrix G ($[\widehat{\zeta}_\sigma^{*s+1}\ \widehat{\zeta}_\sigma^{s+1}\ \widehat{u}_\sigma^{s+1}]^T = G[\widehat{\zeta}_\sigma^{*s}\ \widehat{\zeta}_\sigma^s\ \widehat{u}_\sigma^s]^T$),

$$a_0 + a_1\lambda + a_2\lambda^2 + a_3\lambda^3 = 0 \tag{S25}$$
$$a_3 = (1+T_0+4F\alpha_1)(1+T_b) \tag{S26}$$
$$a_2 = (1+T_0+4F\alpha_1)(-1+T_b) + (-2+4F\alpha_2)(1+T_b) + (4E/A^2)(T_0-T_b) \tag{S27}$$
$$a_1 = (1-T_0+4F\alpha_3)(1+T_b) + (-2+4F\alpha_2)(-1+T_b) + (4E/A^2)(T_0-T_b) \tag{S28}$$
$$a_0 = (1-T_0+4F\alpha_3)(-1+T_b) \tag{S29}$$

where,

$$A = 1 - m\sin^2(\sigma\Delta x/2)$$

205

$$m = \begin{cases} 2/3 & \text{for consistent mass-matrix exact integration} \\ 0 & \text{for lumped mass-matrix nodal integration} \end{cases}$$

$$F = \frac{Cr^2}{A}\sin^2(\sigma\Delta x/2)$$

$$E = AF\cos^2(\sigma\Delta x/2)$$

and we define the following,

210
$$p_0 = a_3 - a_2 + a_1 - a_0 \tag{S30}$$
$$p_1 = 3a_3 - a_2 - a_1 + 3a_0 \tag{S31}$$
$$p_2 = 3a_3 + a_2 - a_1 - 3a_0 \tag{S32}$$
$$p_3 = a_3 + a_2 + a_1 + a_0 \tag{S33}$$
$$\Delta_2 = p_1 p_2 - p_0 p_3 \tag{S34}$$

215   A necessary and sufficient condition for stability, arising from the Routh-Hurwitz criterion of the third-order polynomial resulting from applying the so-called bilinear transform to (S25) (i.e. by the transformation $\lambda = (\Lambda - 1)/(\Lambda + 1)$ which maps the inside of the unit circle of complex numbers λ to the left half plane of Λ), requires that $p_{0,1,2,3} > 0$ and $\Delta_2 > 0$ (Kinnmark, 1986).

To simplify the equations we introduce a weighting scheme that reduces $\alpha_{1,2,3}$ to a single variable, κ. We investigate a
220   centered scheme followed by a non-centered scheme skewed towards the newest time levels.

S1.5.2   Centered scheme

First, the following centered scheme is chosen: $\alpha_1 = \alpha_3 = \kappa$, and $\alpha_2 = 1 - 2\kappa$. This reduces $p_{0,1,2,3}$, Δ_2 to the following,

$$p_0 = 8[1 + F(4\kappa - 1)] \tag{S35}$$
$$p_1 = 8[T_0 + T_b + FT_b(4\kappa - 1) - (E/A^2)(T_0 - T_b)] \tag{S36}$$
225
$$p_2 = 8[F + T_0 T_b] \tag{S37}$$
$$p_3 = 8[FT_b + (E/A^2)(T_0 - T_b)] \tag{S38}$$
$$\Delta_2 = 64[FT_0 + T_0 T_b^2 + T_0^2 T_b + FT_0 T_b^2(4\kappa - 1) - (E/A^2)(T_0 - T_b)(1 + 4F\kappa + T_0 T_b)] \tag{S39}$$

Which leads to the following conditions for stability,

Equation	$Cr \to \infty$	$\tau_0 \to \infty$
p_0	$\kappa \geq 1/4$	$\kappa < 1/4$ and $Cr^2 \leq \frac{1-m}{1-4\kappa}$
p_1	$\kappa \geq 1/4$ and $T_0 \leq 4\kappa T_b$	$Cr^2 \leq 4(m/2 - 1)^2$
p_2	none	none
p_3	none	none
Δ_2	$\kappa \geq 1/4$ and $T_0 \leq T_b$	$Cr^2 \leq 4(m/2 - 1)^2$

230   Thus, for any Cr, the centered scheme is stable if $\kappa \geq 1/4$ and $T_0 \leq T_b$. Note that $\kappa \geq 1/4$ and $T_0 > T_b$ can produce a stable scheme, however, with a restriction on Cr being below a certain value, i.e.: $\kappa \geq 1/4$ and $Cr^2 \leq 4(m/2 - 1)^2$, or $\kappa < 1/4$ and $Cr^2 \leq \frac{1-m}{1-4\kappa}$. The stability constraints are similar to those for the WCE presented by Lynch and Gray (1979), sans the requirement on T_0 (τ_0).

8

S1.5.3 Non-centered scheme

Second, a non-centered scheme skewed towards the $s+1$ and s time levels is chosen: $\alpha_1 = \alpha_2 = \kappa$, and $\alpha_3 = 1 - 2\kappa$. This reduces $p_{0,1,2,3}$, Δ_2 to the following,

$$p_0 = 8[1 + F(1 - 2\kappa)] \tag{S40}$$

$$p_1 = 8\left[T_0 + T_b + F(6\kappa - 2 + T_b(1 - 2\kappa)) - (E/A^2)(T_0 - T_b)\right] \tag{S41}$$

$$p_2 = 8[T_0 T_b + F(1 + 2T_b(3\kappa - 1))] \tag{S42}$$

$$p_3 = 8[FT_b + (E/A^2)(T_0 - T_b)] \tag{S43}$$

$$\Delta_2 = 64[2F^2(T_b^2(-6\kappa^2 + \kappa(5 - T_0) - 1) + 2T_b(9\kappa^2 - 6\kappa + 1) + 3\kappa)$$
$$+ F(T_0 T_b^2 + 12T_0 T_b \kappa - 4T_0 T_b + T_0 + 6T_b^2 \kappa - 2T_b^2) + FT_0 + T_0^2 T_b + T_0 T_b^2] \tag{S44}$$

Which leads to the following conditions for stability,

Equation	$Cr \to \infty$	$\tau_0 \to \infty$
p_0	$\kappa \le 1/2$	$\kappa > 1/2$ and $Cr^2 \le \frac{1-m}{2\kappa-1}$
p_1	$1/3 \le \kappa \le 1/2$ and $\tau_0 \Delta t \le 4(2-m)(3\kappa-1)$	$Cr^2 \le 4(m/2-1)^2$
p_2	$\kappa \ge 1/3$	none
p_3	none	none
Δ_2	$\kappa \ge 1/3$	none

Thus, for any Cr, the non-centered scheme is stable if $1/3 \le \kappa \le 1/2$ and $\tau_0 \Delta t \le 4(2-m)(3\kappa-1)$. Alternatively, Cr-based stability can be achieved if $1/3 \le \kappa \le 1/2$ and $Cr^2 \le 4(m/2-1)^2$, or $\kappa > 1/2$ and $Cr^2 \le \frac{1-m}{2\kappa-1}$.

S2 Model Specifications

In the following sections we detail the pertinent model specifications for the ADCIRC v55 code used in this study. The resulting model setup containing the mesh and input files has been archived in Pringle (2020).

S2.1 Control Settings and Numerical Parameters

1. The momentum equations are used in non-conservative form with the lateral stress tensor in a symmetrical velocity-based form as written in Eqs. (2), (3) of the main manuscript. The full gravity wave term is solved implicitly in the GWCE as written in Eqs. (S14), (S15). In ADCIRC, the aforementioned corresponds to setting the 'fort.15' control file parameter, IM, to a value of 513113 (see: https://wiki.adcirc.org/wiki/IM).

2. The Mercator projection ($p = 2$ in Eq. (S1)) is adopted because of its conformal property. To enable this in an ADCIRC simulation the 'fort.15' control file parameter, ICS, is set to a value of 22 (see: https://wiki.adcirc.org/wiki/ICS).

3. The mesh is rotated internally within ADCIRC to remove the pole singularity (Sect. S1.3). To enable this in an ADCIRC simulation the 'fort.15' control file parameter, ICS, is set to a negative value (i.e, ICS = -22, see: https://wiki.adcirc.org/wiki/ICS). In addition, a 'fort.rotm' input file is provided that indicates the desired rotation (we choose the "Greenland-Antarctica" option listed at https://wiki.adcirc.org/wiki/Fort.rotm).

4. $\kappa = 0.5$ in Eq. (S19) is adopted because it leads to the least restrictive condition on $\tau_0 \Delta t$ in Eq. (S20). The corresponding 'fort.15' control file weighting factors, A00, B00, C00, are set to 0.5, 0.5, 0 (see: https://wiki.adcirc.org/wiki/A00,_B00, _C00).

5. Δt is set to approximately the largest value that enables reliably stable simulations based on experience and trial-and-error. Although the linear CFL condition is satisfied unconditionally, nonlinear terms introduce instabilities on finer meshes in shallow depths. $\Delta t = 120$ s was used for all simulations on the global mesh without local refinement. Δt was

generally reduced for the storm tide simulations on the meshes with local refinement. Hurricane Katrina: Δt = 120 s on the MinEle = 500-m mesh, and Δt = 50 s on the MinEle = 150-m mesh. Super Typhoon Haiyan: Δt = 80 s on the MinEle = 500-m mesh, and Δt = 30 s on the MinEle = 150-m mesh. The corresponding ADCIRC 'fort.15' control file parameter for Δt is DTDP (https://wiki.adcirc.org/wiki/DTDP).

6. We set $\tau_0 = 8/(5\Delta t)$, which is chosen to satisfy the stability criteria for $\tau_0 \Delta t$ in Eq. (S20), with $\kappa = 0.5$ and a safety factor of 0.6 applied to account for any possible 2-D effects. For instance, if Δt = 120 s then τ_0 = 1/75 s^{-1}. The corresponding ADCIRC 'fort.15' control file parameter for τ_0 is TAU0 (https://wiki.adcirc.org/wiki/TAU0).

7. Wetting-drying is enabled but its action is limited to regions with very large tidal ranges or the storm landfall regions because the meshes were built without an overland floodplain in this study. To enable wetting-drying in an ADCIRC simulation, the 'fort.15' control file parameter, NOLIFA, is set to 2 (see: https://wiki.adcirc.org/wiki/NOLIFA).

S2.2 Bathymetric Interpolation

To interpolate the bathymetry from the Digital-Elevation-Model (DEM) structured grid to the unstructured mesh vertices we use a cell-averaging technique native to the OceanMesh2D software, called through the "interp" function wrapper (cf. Roberts et al., 2019). Given the resolution of the meshes and accuracy of the DEM data used in this study, a 5 m floor on the ocean depth was applied.

S2.3 Tidal Potential

The equilibrium tidal potential is prescribed internally in ADCIRC using the analytical formulation presented in Luettich and Westerink (1992, Eq. (27), p. 17). The time-dependent nodal factors and equilibrium arguments for each tidal constituent are computed when constructing the ADCIRC 'fort.15' control file with the "Make_f15" OceanMesh2D function wrapper based on the start and end datetimes of the simulation. Specifically, the nodal factor is set to a constant for each simulation based on the mean datetime, and the equilibrium argument is based on the start datetime. The OceanMesh2D function to compute the nodal factors and equilibrium arguments is adopted from the UTide MATLAB toolbox (Codiga, 2011). In addition, the ADCIRC 'fort.15' control file parameter, NTIP, is set to 1 or 2 (see: https://wiki.adcirc.org/wiki/NTIP), and NTIF is set to the number of tidal constituents used (https://wiki.adcirc.org/wiki/NTIF) – this is automatically handled by the "Make_f15" function.

S2.4 Self-attraction and Loading Tide

We prescribe the self-attraction and loading (SAL) tide by reconstructing the elevation signal from harmonic constituents provided by the FES2014 (Lyard et al., 2006) data assimilated tidal solutions (ftp://ftp.legos.obs-mip.fr/pub/FES2012-project/ data/LSA/FES2014/). These are linearly interpolated from the FES2014 structured grid onto our unstructured mesh vertices. The "Make_f24" OceanMesh2D function is used to perform this process and write out the data into a 'fort.24' ADCIRC input file (see: https://wiki.adcirc.org/wiki/Fort.24_file). To use the SAL information in an ADCIRC simulation, the 'fort.15' control file parameter, NTIP, is set to a value of 2 (see: https://wiki.adcirc.org/wiki/NTIP) – this is automatically handled by the "Make_f24" function.

S2.5 Atmospheric Forcing

In this study atmospheric forcing is either, interpolated from gridded meteorological fields, or reconstructed from the symmetric Holland parametric vortex model internally in ADCIRC during the simulation. The choice of atmospheric forcing type is dictated by the ADCIRC 'fort.15' control file parameter, NWS (see: https://wiki.adcirc.org/wiki/NWS).

To use a single dataset of gridded meteorological fields in GRIB2 file format (e.g., CFSR and CFSv2 as used in this study), NWS is set to 14. To insert a local inset of gridded OceanWeather Inc. (OWI) ASCII file format meteorological fields into the GRIB2 file meteorology, NWS is set to -14. Simultaneously, the WTIMINC 'fort.15' control file parameter is set to the time

Table 1. Calibrated C_{it} values used for each mesh design (refer to Table 2 from the main manuscript for design details).

Variable Mesh Size Parameter	Design Code			
	Ref	A	B	C
MinEle	2.13	2.10	2.02	1.87
TLS	2.13	2.01	1.94	1.65
FL	2.13	2.04	1.95	1.90

interval of the meteorological data in seconds (if NWS = -14, first value is for the GRIB2 meteorology, second value is for the OWI meteorology, see: https://wiki.adcirc.org/wiki/WTIMINC).

310   To use the symmetric Holland parametric vortex model, NWS is set to 8, a 'fort.22' meteorology control file is supplied (see: https://wiki.adcirc.org/wiki/Fort.22_file_format#NWS_.3D_8), and we choose the 'fort.15' control file parameter, BLAdj, to be 0.78 (see: https://wiki.adcirc.org/wiki/YYYY_MM_DD_HH24_StormNumber_BLAdj).

S2.6   Internal Tide Wave Drag

The "Calc_IT_Fric" OceanMesh2D function is used to compute the internal tide wave drag tensor, $\mathcal{C}$ offline using the local-generation formulation, incorporating saturation at supercritical topography, and a cutoff depth of 250 m below which $\mathcal{C}$ is set
315   to zero (cf. Pringle et al., 2018b). Critical to this computation is the determination of the topographic gradients. To perform this calculation the OceanMesh2D "interp" function wrapper is used prior to the "Calc_IT_Fric" function call. "interp" employs a cell-averaging type technique where the magnitude of the topographic gradients at the mesh vertices are computed as the root-mean-square of the topographic gradients directly computed on the DEM points located within a region determined by a measure of the local mesh size. The sign of the topographic gradient is then determined by the sign of the gradient of the
320   interpolated bathymetry on the mesh vertices. The aim of this interpolation strategy is to ensure that sub-grid information of the topographic gradient on the original DEM is preserved. In this way the form of the internal tide wave drag tensor used here can be thought of as a hybrid of the Jayne and St. Laurent (2001) sub-grid roughness method and Lyard et al. (2006); Zaron and Egbert (2006) gradient-based methods.

The internal tide wave drag tensor contains a free parameter C_{it} (see the main manuscript). In this study we consider C_{it} to
325   be a globally constant calibration coefficient that should be tuned so that the model simulation has the correct total barotropic tidal energy in the deep ocean ($h > 1$ km). For this purpose we use the total available tidal potential energy of the 5-constituent tidal signal,

$$\text{APE}_{t|tot} = \frac{\rho g}{4} \iint \sum_{k=1}^{5} A_k^2 \, dA \tag{S45}$$

where A is the tidal amplitude, and k indicates the arbitrary constituent number (amongst the five leading constituents, M_2, S_2,
330   N_2, K_1, O_1). C_{it} is varied (to a precision of ± 0.01) until the simulated $\text{APE}_{t|tot}$ in the deep ocean matches that of the TPXO9-Atlas (= 153 PJ). The resulting C_{it} values for the various mesh designs are shown in Table 1. A map of the infinity-norm of the $\mathcal{C}$ tensor on the reference mesh is shown in Fig. S2.

To use the internal tide wave drag tensor in an ADCIRC simulation, the data is written out as an "internal_tide_friction" 'fort.13' input file attribute (see: https://wiki.adcirc.org/wiki/Fort.13_file#Internal_Tide_Energy_Conversion).

335 ### S2.7   Quadratic Bottom Friction

For all mesh designs, C_f in τ_b (refer to main manuscript) is set to 0.0025 everywhere except under the Antarctic and Greenland ice shelves where C_f is doubled (c.f. Zaron, 2019), and in the Indian and Western Pacific Oceans where values from Pringle et al. (2018a) are used (Fig. S3). In particular, small values of C_f (ranging between 0.00075 and 0.002) in the Yellow Sea are important to reduce the tidal error here (Lefevre et al., 2000; Pringle et al., 2018a). Other variations of C_f outside of
340   these regions would likely also further reduce the tidal error but the determination of a suitable unified framework to calibrate spatially varying C_f globally is left for future work.
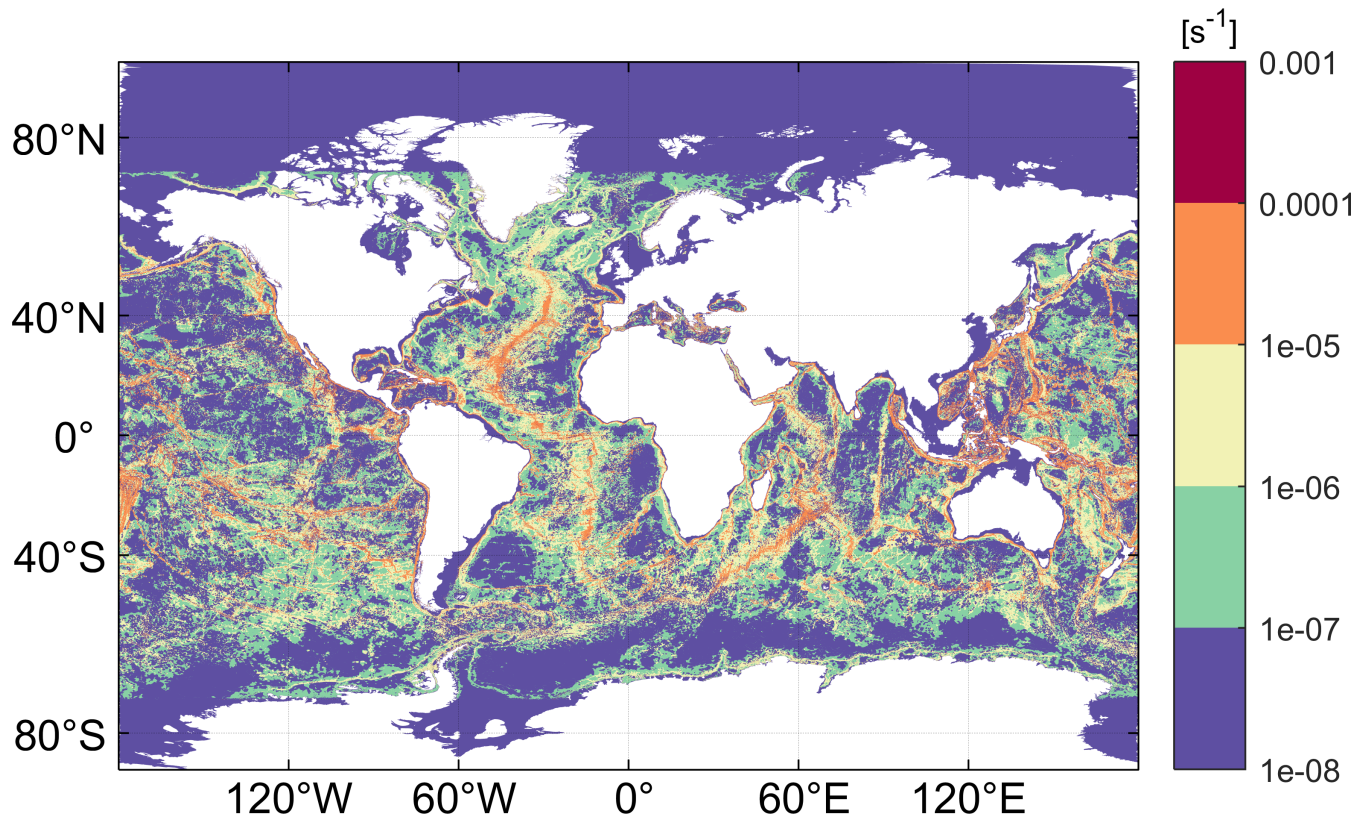
Figure S2. Map of the infinity-norm of the internal tide wave drag tensor, $\mathcal{C}$ on the reference mesh.

To use quadratic bottom friction in an ADCIRC simulation, the NOLIBF 'fort.15' control file attribute is set to 1 (see: https://wiki.adcirc.org/wiki/NOLIBF), and the "quadratic_friction_coefficient_at_sea_floor" 'fort.13' input file attribute is used to specify spatially varying C_f (see: https://wiki.adcirc.org/wiki/Fort.13_file#Quadratic_Friction_coefficient).

S2.8 Lateral Mixing

The lateral mixing coefficient, ν_t is calculated through the Smagorinsky turbulence closure model with a coefficient of 0.2 (Dresback et al., 2005). Model results were insensitive to this coefficient for the values we tested (0.05, 0.10, 0.20) but it can help for model stability to use a larger value.

To use the Smagorinksy model in an ADCIRC simulation, the ESLM 'fort.15' control file attribute is set equal to the negative value of the Smagorinksy coefficient (i.e., ESLM = -0.2) (see: https://wiki.adcirc.org/wiki/ESLM).
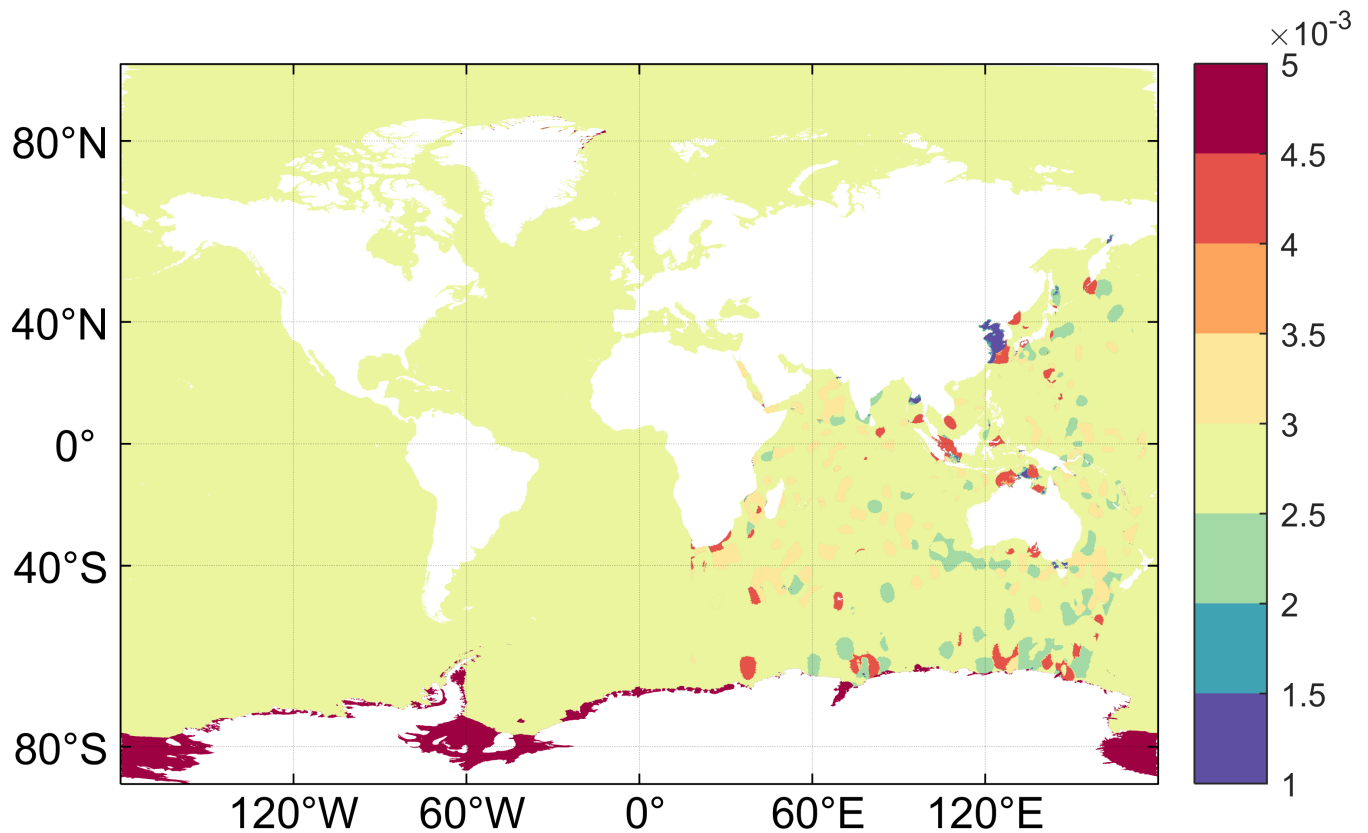
Figure S3. Map of spatially varying bottom friction coefficients, C_f on the reference mesh.

References

Castro, M. J., Ortega, S., and Parés, C.: Reprint of: Well-balanced methods for the shallow water equations in spherical coordinates, Computers and Fluids, 169, 129–140, https://doi.org/10.1016/j.compfluid.2018.03.052, https://doi.org/10.1016/j.compfluid.2017.08.035, 2018.

Chen, C., Gao, G., Zhang, Y., Beardsley, R. C., Lai, Z., Qi, J., and Lin, H.: Circulation in the Arctic Ocean: Results from a high-resolution coupled ice-sea nested Global-FVCOM and Arctic-FVCOM system, Progress in Oceanography, 141, 60–80, https://doi.org/10.1016/j.pocean.2015.12.002, http://dx.doi.org/10.1016/j.pocean.2015.12.002, 2016.

Codiga, D. L.: Unified Tidal Analysis and Prediction Using the UTide Matlab Functions, Tech. Rep. 01, Graduate School of Oceanography, University of Rhode Island, Narragansett, RI, https://doi.org/10.13140/RG.2.1.3761.2008, 2011.

Comblen, R., Legrand, S., Deleersnijder, E., and Legat, V.: A finite element method for solving the shallow water equations on the sphere, Ocean Modelling, 28, 12–23, https://doi.org/10.1016/j.ocemod.2008.05.004, http://dx.doi.org/10.1016/j.ocemod.2008.05.004, 2009.

Dresback, K. M. and Kolar, R. L.: An implicit time-marching algorithm for shallow water models based on the generalized wave continuity equation, International Journal for Numerical Methods in Fluids, 36, 925–945, https://doi.org/10.1002/fld.157.abs, 2002.

Dresback, K. M., Kolar, R. L., and Dietrich, J. C.: On the form of the momentum equation for shallow water models based on the generalized wave continuity equation, Advances in Water Resources, 28, 345–358, https://doi.org/10.1016/j.advwatres.2004.11.011, 2005.

Foreman, M. G. G.: An Anaysis of the "Wave Equation" Model for Finite Element Tidal Computations, Journal of Computational Physics, 52, 290–312, 1983.

Gray, W. G. and Lynch, D. R.: On the control of noise in finite element tidal computations: A semi-implicit approach, Computers and Fluids, 7, 47–67, https://doi.org/10.1016/0045-7930(79)90005-7, 1979.

Hervouet, J.-M.: Equations of free surface hydrodynamics, in: Hydrodynamics of Free Surface Flows: Modelling with the Finite Element Method, chap. 2, pp. 5–75, John Wiley & Sons, Ltd, https://doi.org/10.1002/9780470319628.ch2, https://onlinelibrary.wiley.com/doi/abs/10.1002/9780470319628.ch2, 2007.

Jayne, S. R. and St. Laurent, L. C.: Parameterizing tidal dissipation over rough topography, Geophysical Research Letters, 28, 811–814, https://doi.org/10.1029/2000GL012044, http://doi.wiley.com/10.1029/2000GL012044, 2001.

Kinnmark, I. P.: The Shallow Water Wave Equations: Formulation, Analysis and Application, vol. 15 of *Lecture Notes in Engineering*, Springer Berlin Heidelberg, Berlin, Heidelberg, https://doi.org/10.1007/978-3-642-82646-7, http://link.springer.com/10.1007/978-3-642-82646-7, 1986.

Kinnmark, I. P. and Gray, W. G.: A Two-Dimensional Analysis of the Wave Equation Model for Finite Element Tidal Computations, International Journal for Numerical Methods in Engineering, 20, 369–383, 1984.

Kolar, R. L., Gray, W. G., Westerink, J. J., and Luettich, R. A.: Shallow water modeling in spherical coordinates: Equation formulation, numerical implementation, and application: Modélisation des équations de saint-venant, en coordonnées sphériques: Formulation, resolution numérique et application, Journal of Hydraulic Research, 32, 3–24, https://doi.org/10.1080/00221689409498786, 1994a.

Kolar, R. L., Westerink, J. J., Cantekin, M. E., and Blain, C. A.: Aspects of Nonlinear Simulations using Shallow-water Models based on the Wave Continuity Equation, Computers & Fluids, 23, 523–538, 1994b.

Le Bars, Y., Lyard, F., Jeandel, C., and Dardengo, L.: The AMANDES tidal model for the Amazon estuary and shelf, Ocean Modelling, 31, 132–149, https://doi.org/10.1016/j.ocemod.2009.11.001, http://dx.doi.org/10.1016/j.ocemod.2009.11.001, 2010.

Lefevre, F., Provost, C. L., and Lyard, F. H.: How can we improve a global ocean tide model at a region scale? A test on the Yellow Sea and the East China Sea, Journal of Geophysical Research: Oceans, 105, 8707–8725, https://doi.org/10.1029/1999JC900281, 2000.

Luettich, R. A. and Westerink, J. J.: ADCIRC: an advanced three-dimensional circulation model for shelves coasts and estuaries, report 1: theory and methodology of ADCIRC-2DDI and ADCIRC-3DL, Dredging Research Program, Tech. rep., DRP-92-6, U.S. Army Engineers Waterways Experiment Station, Vicksburg, MS, 1992.

Luettich, R. A. and Westerink, J. J.: Formulation and Numerical Implementation of the 2D/3D ADCIRC Finite Element Model Version 44.XX, Tech. rep., University of North Carolina at Chapel Hill & University of Notre Dame, 2004.

Lyard, F., Lefevre, F., Letellier, T., and Francis, O.: Modelling the global ocean tides: modern insights from FES2004, Ocean Dynamics, 56, 394–415, https://doi.org/10.1007/s10236-006-0086-x, http://link.springer.com/10.1007/s10236-006-0086-x, 2006.

Lynch, D. R. and Gray, W. G.: A Wave Equation Model for Finite Element Tidal Computations, Computers & Fluids, 7, 207–228, 1979.

Pringle, W. J.: Global Storm Tide Modeling on Unstructured Meshes with ADCIRC v55 - Simulation Results and Model Setup, https://doi.org/10.5281/zenodo.3911282, 2020.

Pringle, W. J., Wirasaet, D., Suhardjo, A., Meixner, J., Westerink, J. J., Kennedy, A. B., and Nong, S.: Finite-Element Barotropic Model for the Indian and Western Pacific Oceans: Tidal Model-Data Comparisons and Sensitivities, Ocean Modelling, 129, 13–38, https://doi.org/10.1016/j.ocemod.2018.07.003, https://linkinghub.elsevier.com/retrieve/pii/S146350031830026X, 2018a.

Pringle, W. J., Wirasaet, D., and Westerink, J. J.: Modifications to Internal Tide Conversion Parameterizations and Implementation into Barotropic Ocean Models, EarthArXiv, p. 9, https://doi.org/10.31223/osf.io/84w53, 2018b.

Roberts, K. J., Pringle, W. J., and Westerink, J. J.: OceanMesh2D 1.0: MATLAB-based software for two-dimensional unstructured mesh generation in coastal ocean modeling, Geoscientific Model Development, 12, 1847–1868, https://doi.org/10.5194/gmd-12-1847-2019, 2019.

Tanaka, S., Bunya, S., Westerink, J. J., Dawson, C., and Luettich, R. A.: Scalability of an Unstructured Grid Continuous Galerkin Based Hurricane Storm Surge Model, Journal of Scientific Computing, 46, 329–358, https://doi.org/10.1007/s10915-010-9402-1, http://link.springer.com/10.1007/s10915-010-9402-1, 2011.

Westerink, J. J., Luettich, R. A., Baptists, A. M., Scheffner, N. W., and Farrar, P.: Tide and Storm Surge Predictions Using Finite Element Model, Journal of Hydraulic Engineering, 118, 1373–1390, https://doi.org/10.1061/(ASCE)0733-9429(1992)118:10(1373), http://ascelibrary.org/doi/10.1061/{%}28ASCE{%}290733-9429{%}281992{%}29118{%}3A10{%}281373{%}29, 1992.

Zaron, E. D.: Simultaneous Estimation of Ocean Tides and Underwater Topography in the Weddell Sea, Journal of Geophysical Research: Oceans, 124, 3125–3148, https://doi.org/10.1029/2019JC015037, 2019.

Zaron, E. D. and Egbert, G. D.: Estimating Open-Ocean Barotropic Tidal Dissipation: The Hawaiian Ridge, Journal of Physical Oceanography, 36, 1019–1035, https://doi.org/10.1175/JPO2878.1, http://journals.ametsoc.org/doi/abs/10.1175/JPO2878.1, 2006.